Stiffening of organosilicate glasses by organic cross-linking

Han Li[a], Jan M. Knaup[b,c], Efthimios Kaxiras[a,b,c], Joost J. Vlassak[a] *

[a] *School of Engineering and Applied Sciences, Harvard University*

Cambridge, Massachusetts, 02138, USA

[b] *Department of Physics, Harvard University, Cambridge MA 02138, USA*

[c] *Ecole Polytechnique Fédérale de Lausanne*

Station 12, CH-1015 Lausanne, Suisse

Abstract –

Atomistic simulations show that organosilicates, used as low-permittivity dielectric materials in advanced integrated circuits, can be made substantially stiffer than amorphous silica, while maintaining a lower mass density. The enhanced stiffness is achieved by incorporating organic cross-links to replace bridging oxygen atoms in the silica network. To elucidate the mechanism responsible for the enhanced stiffness, the conformational changes in the network upon hydrostatic and shear loading are examined. The structural and mechanical impact of terminal methyl groups is also assessed quantitatively and compared with continuous random network theory.

Keywords:

*Corresponding author. e-mail: vlassak@esag.harvard.edu

1. Introduction

Continued miniaturization of integrated circuits requires interconnect insulator materials with reduced dielectric constant (‘*k*’) [1-3]. Organosilicate glasses (OSG) are a family of organic-inorganic hybrid materials that possess a silica-like backbone structure with *k* values typically in the range of 2.7~3 compared to 3.9~4 for silica. Already implemented in the 90nm and 65nm nodes [4, 5], OSG-type materials are also widely regarded as the most promising low-*k* dielectrics for future integrated circuit technologies. The low dielectric constant is achieved by introducing organic terminal groups into the silica network. This modification decreases the OSG density and lowers the bond polarizability, both beneficial for the dielectric performance. The dielectric constant is reduced even further by making the OSG porous. From a mechanical point of view, the terminal groups disrupt the glass network and degrade the mechanical integrity of the materials. Successful integration into integrated circuits of OSG with high porosity levels imposes stringent demands on the mechanical properties of the OSG to better withstand the rigors of the fabrication process.

The mechanical properties of amorphous solids are determined essentially by their covalent network structure [6-11]. Experiments have demonstrated that the elastic modulus and fracture toughness of as-deposited OSG thin films can be improved by broadband ultraviolet (UV) irradiation and thermal treatments [7, 8, 10]. Such improvements are associated with a more densely cross-linked network structure attained by removing terminal groups and by forming networking bonds [8, 10, 12]. The same principle can also be used to strengthen films during film deposition: By engineering the precursor monomers and synthesis conditions, hydrocarbon molecules can be incorporated into the material matrix as network-forming units rather than as terminal groups, resulting in a network that is less disrupted and has improved strength [9, 11, 13, 14]. To better understand this strengthening mechanism, quantitative molecular modeling is indispensable.

Using constraint theory, amorphous solids have been modeled as continuous random networks [6, 15]. Each atom in the network is covalently bonded to its nearest neighbors, and subject to constraints associated with bond stretching and bending. In such networks, all bonds are viewed as equivalent and the network is quantified by the average coordination number of all network-forming atoms, termed the network connectivity <r>. He and Thorpe have shown by means of numerical simulations that the elastic properties of random networks are determined by their network connectivity value [15]. Rigidity

percolation occurs and the system transforms from floppy (under-constrained) to stiff (over-constrained) as the connectivity number exceeds a threshold value $<r>_c$. The constraint theory argument, however, may not be directly applicable to complex materials such as organosilicates, where different covalent bonds and non-bond interactions also need to be accounted for. To this end, atomistic models with sophisticated interatomic potentials have been developed [16-18]. A popular approach to constructing models for OSG-like materials consists of modifying the backbone structure of amorphous silica [19-22]. Molecular dynamics (MD) simulations using these atomistic models have been able to reproduce experimental observations to a certain extent [19-22], but a fundamental mechanistic understanding of the structure-property relationship is still lacking. Further studies are needed to develop critical insight required to guide material developments.

The objective of this paper is to explore systematically and quantitatively how the mass density and mechanical properties of OSG are correlated with its network structure. To delineate the respective role of various bridging and terminal groups, two classes of OSG models are considered. The first class of models consist of a Si–O–Si and Si–CH_2–Si network without terminal groups – we refer to them as type-I OSG models. The second class of models, or type-II OSG models, have only Si–O–Si bonds in the network, but terminal groups (–OH or –CH_3) are allowed. We demonstrate the potential of synthesizing stiffer-than-silica OSG-type materials by organic cross-linking and by limiting the terminal group population. To elucidate the mechanism for the enhanced stiffness, network deformation upon hydrostatic and shear loading is analyzed. The implications for developing porous ultralow-k dielectrics with improved mechanical properties are discussed.

2. Model construction

Construction of the OSG models involves two major steps as illustrated in Fig.1. A 64-atom amorphous silicon model that was generated earlier by slowly quenching of liquid silicon followed by a simulated annealing [16], and is used as the starting structure in this study. The interatomic potential that was used for this simulation accounts for the dependence of chemical bonding (bond order, hybridization and so forth) on the local coordination number, and has been demonstrated to generate realistic amorphous silicon structures [16].

In step 1, the amorphous silicon supercell (Fig.2a) is first expanded in all three dimensions by a factor of 1.338 to ensure that the derivative silica model will have a

density of 2.2 g/cm^3 before structural relaxation. After the expansion, all Si–Si pairs are replaced by Si–O–Si. The Si–O–Si bond angle is initially set at 150^o with random orientation about the former Si–Si bonds. The resultant silica structure (Fig.2b) is then relaxed by potential energy minimization. More details on the interatomic potential used in this study for the relaxation and the MD simulations are provided in the next section. The supercell is allowed to change shape and size without any structural constraints other than periodic boundary conditions in the three directions.

In step 2, we derive type-I and type-II OSG models based on the relaxed amorphous silica (a-silica) model using the following procedure. For type-I models, a fraction of the bridging oxygen atoms in the silica backbone structure are replaced by methylene groups (Fig.2c), such that the network connectivity remains unchanged compared to silica (methylene group is regarded as one "atom"). For type-II models, a number of Si–O–Si units in the silica structure are converted into pairs of Si–T units by breaking the Si–O bonds and replacing the oxygen atom with two 'T' groups, where 'T' denotes a terminal group that can be either –OH or –CH_3. The selection of terminal groups is guided by experiments [8, 23, 24]. These terminal groups are randomly oriented provided no overlapping between atoms occurs. Before carrying out the MD simulations, the structures are relaxed by potential energy minimization (Fig.2d). For statistical purpose, five configurations in which terminal positions are randomly selected are constructed for each composition. Preliminary simulations using OSG models that were eight times as large indicate that finite size effects are insignificant for the properties investigated in this study. The results presented in this paper by default refer to the 64-Si models unless otherwise specified.

3. Simulation protocol

The MD simulations were performed using the COMPASS force field [25]. COMPASS is an empirical many-body potential that has been extensively parameterized using *ab initio* calculations and experimental data, with a functional form that includes covalent terms as well as long-range, non-bond interactions (i.e., van der Waals and electrostatic forces).

The MD simulations in this study consist of two sequential steps: equilibration and property sampling. A typical equilibration starts with 20 ps of NVT dynamics during which volume and temperature are kept constant, followed by NPT dynamics during which pressure and temperature are maintained constant. Preliminary simulations showed that the 20-ps NVT step prevents incidental trajectory divergence in the subsequent NPT

simulation. Similar procedures have also been used by other researchers [26]. The NPT step continues until the energy and temperature of the system reach a steady state for more than 100 ps, and lasts from 200 to 1600 ps depending on the model. System temperature is maintained at 298 K using Andersen's thermostat [27]. In the NPT ensemble, the external stress is controlled by the Parrinello-Rahman method [28]. Hydrostatic pressures and shear stresses are applied to the OSG supercell to simulate volumetric and shear deformation, respectively. After equilibration the NPT simulation is continued for another 20 ps to generate trajectories for extracting time-averaged structural and mechanical properties. The complete 6x6 elastic stiffness matrix can be obtained following standard procedure [29]. The bulk modulus and shear modulus are calculated from the elastic constants according to [29]

$$B = \left(C_{11} + C_{22} + C_{33} + 2C_{12} + 2C_{13} + 2C_{23}\right)/9 \quad (1)$$

$$G = \left(C_{11} + C_{22} + C_{33} + 2C_{44} + 2C_{55} + 2C_{66} - C_{12} - C_{13} - C_{23}\right)/15 \quad (2)$$

In all simulations, periodic boundary conditions are imposed in all the three directions. Electrostatic potential summation is conducted using Ewald's method [30] with a cutoff distance of 12.5 angstrom. The velocity-Verlet algorithm based on the original Verlet algorithm [31] is used to integrate Newton's equations of motion with a time step of 1 fs. Extensive preliminary simulations were conducted to ensure that the structure was sufficiently equilibrated and convergent results were obtained under the specified conditions. The simulations were performed using the software package 'Materials Studio' [32].

4. Results and discussion

4.1 Type-I OSG: effect of organic bridging units

4.1.1 Structural and elastic properties at zero pressure

Our simulation results show that the incorporation of $–CH_2–$ as cross-links in the silica network has a pronounced impact on the structure and mechanical properties of the resultant organosilicates. For the a-silica model, the calculated mass density and the Si–O–Si angle distribution agree well with experimental measurements on silica glasses [33-35]. The O–Si–O angle exhibits a tight distribution with a maximum at 109.4º, indicating nearly perfect SiO_4 tetrahedra. As the silica network is chemically modified, the density of type-I OSG first increases slightly, and then decreases rather quickly with further $–CH_2–$ introduction (Fig.3a). The overall trend is in reasonable agreement with predictions from density functional theory based on the tight-binding (DFTB) method [36]. Evidently,

the introduction of methylene cross-links reduces the material density significantly. Note that the density results calculated using models eight times as large closely overlap with results for the smaller OSG models, indicating that the finite size does not affect the density calculations significantly.

The change in material density is due to (1) the CH_2 group is 12.5% lighter than an oxygen atom, and (2) the evolution of the various bond lengths and angles as the silica structure is modified (Fig.3b and 3c). The Si–O–Si and Si–C–Si bonds are relatively flexible in bending, and hence are most sensitive to changes in the composition. By contrast, the O–Si–O, C–Si–C and C–Si–O bonds within the individual silicon tetrahedral units are very stiff and the corresponding bond angles remain essentially unchanged. A closer look reveals that the mean Si–C–Si angle increases monotonically as the $–CH_2–$ concentration increases (Fig.3b). The same holds true for the Si–O and Si–C bond length (Fig.3c), although the relative variations are much smaller. These structural changes expand and open up the network, thus reducing the density. The mean Si–O–Si bond angle goes through a minimum with increasing $–CH_2–$ population (Fig.3b); this minimum corresponds to the OSG composition with the largest density (CH_2/Si=~0.3). When $–CH_2–$ is dilute in the network, the decrease in Si–O–Si angle counteracts the effect of the Si–C–Si, Si–C and Si–O bonds; after reaching the composition of minimum Si–O–Si angle, all structural changes act to reduce the material density. Therefore, the glass network enlarges more effectively, leading to a fast decrease in density with increasing $–CH_2–$ population.

Introducing $–CH_2–$ groups as bridging units changes the elastic properties of the OSG. Indeed, the bulk modulus gradually increases from the value of pure silica (~39.5 GPa) to 59.3 GPa as half of the oxygen atoms are replaced (see Fig.4a). Further increasing the $–CH_2–$ content continues the trend, but at a lower rate; an additional enhancement of only 16% can be obtained when the remaining oxygen atoms are completely substituted by $–CH_2–$ groups. Calculations using DFTB reproduce a similar trend for the bulk modulus [36]. By contrast, the shear modulus of the OSG model depends only slightly on the $–CH_2–$ population without significant change from the silica value as shown in Fig.4a. Figure 4b plots Young's modulus of type-I OSG as a function of the CH_2/Si ratio, along with results obtained using DFTB [36] and the MM3 force field [19]. Evidently, our results are consistent with the calculation from density function theory, although a more significant increase in elastic modulus (bulk, shear and Young's modulus) is obtained for the latter. The increased stiffness with $–CH_2–$ concentration is caused by the higher bending rigidity of the Si–C–Si bonds than that of Si–O–Si bonds,

and will be explained further in section 4.1.2. Comparison with the results in ref. [19] is difficult, primarily because of the large scatter in the modulus values reported in this reference; no clear trend can be discerned. In general, we note that heavily distorted models or models that are insufficiently relaxed can give rise to much reduced modulus values. This reduction in stiffness has been attributed to the fact that the network bond configuration is energetically less stable than well-relaxed models and thus more easily deformed [8, 10].

While the observation that the mechanical behavior of OSG is sensitive to the precise network structure is well known from experiments [7, 8, 37], the finding that it may be possible to produce OSG materials that are less dense but substantially stiffer than silica is somewhat unexpected. The increased stiffness contrasts with the commonly held perception that organic crosslinking renders the network more compliant.

4.1.2 Bond deformation under hydrostatic and shear loading

To better understand the elastic properties of type-I OSG and in particular the mechanism responsible for the enhanced stiffness, all possible bond stretching and bending molecular deformation modes are investigated under hydrostatic and pure shear loading conditions. For simplicity, we focus our discussion on the materials at either end of the composition spectrum, i.e., SiO_2 and $Si(CH_2)_2$.

The evolution of the SiO_2 network structure under hydrostatic pressures is documented in the left panels of Fig.5. It is evident from the plots that the bulk deformation of SiO_2 is mostly associated with a change in the Si–O–Si bond angle distribution. By comparison, the distributions of the Si–O bond length and the O–Si–O angle remain nearly unchanged. Indeed, the relative variation of the mean Si–O–Si angle per unit strain is much larger than the corresponding variation for the O–Si–O angle or the Si–O length (Fig.5 left-bottom). Thus deformation of SiO_2 under hydrostatic loading is accommodated mainly by the bending of the Si–O–Si bonds connecting nearly rigid SiO_4 tetrahedra.

The SiO_2 network structure evolves rather differently under shear loading. A salient feature of this mode of deformation is that none of the bond length or angle distributions is significantly affected. More detailed information is required to describe the mechanism responsible for shear deformation, including information on (1) how individual bonds are deformed before and after the shearing, and on (2) how the relative deformation of the bonds is distributed. As an example, Fig.6a plots the distribution of the relative change in angle for all the Si–O–Si bonds upon shear loading, where the

undeformed network was used as the reference configuration. Clearly, the distribution is symmetric about zero angle change, i.e., the number of Si–O–Si bond angles that become larger upon shearing equals the number of Si–O–Si bond angles that decrease by the same amount. Consequently, the overall Si–O–Si angle distribution remains unchanged. This is not surprising as shear deformation can be decomposed into equal amounts of tensile and compressive strain along two mutually perpendicular axes. For comparison, Fig.6b and 6c shows the distributions of the relative change of the Si–O–Si bond angles upon hydrostatic compression and tension, respectively. Even though the distributions are largely symmetric, there is now a definite offset. The value of this offset is determined by the hydrostatic pressure, and is equal to the change in the mean Si–O–Si bond angle as plotted in Fig.5. A similar analysis for all types of bonds in the network shows that bending of the Si–O–Si bonds contributes the most to shear deformation of silica. This is so because of the greater flexibility of these bonds compared to stretching of the Si–O bond or bending of the O–Si–O bond.

In $Si(CH_2)_2$, the Si–C–Si bond angle and the Si–C bond length distributions are much more affected by external loads (hydrostatic or shear) than the C–Si–C angle distribution. This is illustrated for hydrostatic loading in the right panels of Fig.5. The elastic deformation of the network is accommodated primarily by bending of the Si–C–Si bonds and by stretching of the Si–C bonds. The Si–C stretching occurs in response to external loading because the Si–C–Si cross-links have a larger bending stiffness than the Si–O–Si bonds in silica. This larger bending stiffness also explains the finding that the bulk modulus of type-I OSG increases with $–CH_2–$ population, and it is consistent with the trend of our previous DFTB calculations [36]. Indeed, according to DFTB, the Si–C–Si bonds have an even larger bending stiffness, thus causing a steeper rise in the network stiffness compared with the result obtained from the COMPASS force field (Fig.4).

The differences between the MD and DFTB results, visible in Figs. 3 and 4, are mainly due to two factors: (1) the COMPASS force field allows for some deformation of the $Si–CH_2–Si$ bonds while they are nearly rigid in DFTB; (2) the DFTB calculations are static simulations at 0K while the MD simulations are performed at finite temperature. The former effect explains the lower elastic moduli obtained for $Si(CH_2)_2$ in the MD simulations. The kinks in the density and modulus curves upon addition of small amounts of $–CH_2–$ are an effect of different thermal behavior of silica and $Si(CH_2)_2$. That is, different thermal expansion coefficients and different thermal dependencies of the elastic coefficients. Considering the stiffness of $Si–CH_2–Si$ units, it is difficult to decide which method provides a more accurate description of reality. To this end, further comparison

with results from more sophisticated DFT functionals would be valuable, albeit we expect the overall feature to remain the same. Note that standard GGA DFT functionals tend to systematically underestimate the bulk moduli, hence are not suitable for use as a reference.

In summary, the MD simulation results reveal that bending of the Si–O–Si angle is the dominant deformation mechanism for a-silica; for $Si(CH_2)_2$, both Si–C–Si bond bending and Si–C stretching occur because of the larger bending stiffness of the Si–C–Si bonds as compared to the Si–O–Si bonds.

4.2 Type-II OSG: effect of terminal groups

Type-II OSG materials contain a number of terminal groups interrupting the network structure. Here we investigate the effects of $–CH_3$ and –OH terminal groups as inspired by experiments [8, 23, 24]. To introduce terminal groups, a fraction of the Si–O–Si units are broken, and the bridging oxygen atom in each unit is replaced by two terminal groups. The disrupted network structure can be described through use of the network connectivity number <*r*>, which is defined as the average coordination number per network forming atom [15]. The connectivity number of type-I OSG is the same as for a-silica (<*r*>=2.67) regardless of the $–CH_2–$ population. The value of <*r*> for type-II OSG is related to the number of terminal groups through

$$\langle r \rangle = \frac{r_{Si} \cdot N_{Si} + r_O \cdot N_O + r_T \cdot N_T}{N_{Si} + N_O + N_T} = \frac{4 \cdot N_{Si} + 2 \cdot \left(2N_{Si} - N_T/2\right) + N_T}{N_{Si} + \left(2N_{Si} - N_T/2\right) + N_T} = \frac{16}{6 + N_T/N_{Si}} \quad (3)$$

where $N_{Si,O,T}$ is the number of silicon atoms, bridging oxygen atoms, or terminal groups as denoted by the subscript, and $r_{Si,O,T}$ is the respective coordination number. Each terminal group is considered as a single atom in the calculation.

As more terminal groups are introduced, the network structure is increasingly disrupted and the network connectivity <*r*> decreases. The MD simulations show that both the bulk modulus and the shear modulus of type-II OSG are reduced significantly (Fig.7a), while Poisson's ratio increases (Fig.7b). Figure 7(c) further shows that the density decreases with decreasing <*r*> as more free volume is generated by the terminal groups. That the density of OSG decreases faster with <*r*> for $–CH_3$ terminal groups than for –OH groups is caused by the relatively larger free volume associated with the methyl group.

The trends of the elastic properties and density with <*r*> agree well with experimental reports on similar OSG materials in the literature [7, 8, 10]. In fact, it has been consistently reported by a number of researchers that UV irradiation can stabilize

the OSG network through local bond rearrangement, and that it can promote further development of network cross-linking by severing loose terminal groups [7, 8, 10]. Associated with these structural changes are a larger network connectivity, an increase in elastic modulus and in density [7, 8, 10], and a reduction in Poisson's ratio [10]. For a more quantitative picture, we compare our simulations with experimental results reported in the literature by several research groups [7, 10, 38, 39]. Figure 8(a) plots the plane-strain modulus of a range of OSG materials as a function of mass density. Clearly, the MD models for type-II OSG with methyl terminal groups are in line with the experimental OSG results at the low-density end, and with the amorphous silica results at the high-density end. Moreover, the simulation results provide a useful reference outside the material space currently accessible.

We also compare our results with MD simulations that have been reported by Tajima et al. [20] and by Yuan et al. [40]. Tajima's OSG models are similar to ours, but these researchers allow both $-CH_3$ and –H terminals at the same time. In Tajima's models, the relative concentrations of the terminal groups are varied to best match the chemical composition and density obtained from experimental measurements, and simulations are performed with the MM3 force field [41]. Yuan's model is based on a backbone framework that is initially an ordered cubic grid [40], and uses the same force field as in this study. Figure 8(b) plots the Young's moduli of the material models versus density. Our results agree well with those of Tajima [20, 21], even though Tajima's models contain a small amount of –H terminal groups and a different force field was used for the simulations. Our results differ significantly from those reported by Yuan [40], probably because of the rather different method of constructing the models. More specifically, the network structure in our OSG models is similar to that of amorphous silica, while Yuan's model uses a network structure based on a cubic lattice. Our simulations also use periodic boundary conditions, while Yuan imposes no periodical boundary conditions.

We further compare our results with continuous random network theory. Numerical simulations based on constraint theory show that the elastic properties of a continuous random network are determined almost entirely by the network connectivity $\langle r \rangle$ [15]. Our results demonstrate that the specific terminal groups also play a significant role. For instance, Fig. 7a shows that the elastic moduli (bulk and shear) decrease more slowly with decreasing $\langle r \rangle$ for CH_3-terminated OSG than for OH-terminated OSG. Factors that are not included in continuous random network theory but that may be important for the stiffness of the network include (1) the number of networking bonds per unit area, which is different for the different terminal groups, and (2) long-range non-

bond interactions that are different for OSG models with different terminal groups. Considering that the density of OH-terminated OSG is larger and the elastic moduli are smaller than for CH_3-terminated OSG of the same connectivity (Fig.8a-c), we conclude that the long-range interactions are indeed important.

Another important difference between the MD simulations and constrained random network theory relates to rigidity percolation. According to classical constraint theory, a network is over-constrained when the number of constraints imposed by the network bonds exceeds the number of degrees of freedom. If the number of constraints is smaller than the degrees of freedom, the network is under-constrained and the stiffness decreases rapidly. This transition occurs at the rigidity percolation threshold. The percolation threshold is generally not a constant but a function of the fraction of onefold-coordinated atoms in the network, x_1, through $\langle r \rangle_c = 2.4 - 0.4 \cdot x_1$ [15]. For the most disrupted model in this study, the percolation threshold $\langle r \rangle_c$ predicted by random network model is 2.26. Our MD simulations, however, show that there is no sudden change in stiffness near the theoretical percolation threshold. Instead the stiffness of the OSG networks decreases gradually over a range of <r> values. We ascribe this behavior to the long-range non-bond interactions that are present in the MD simulations but that are not considered in the continuous random network model.

4.3 Implication for the synthesis of low-k dielectrics with improved rigidity

Dense OSG materials that rely on methyl groups to reduce their dielectric constants have a Young's modulus that is less than one third the modulus of silica. To further reduce the dielectric constant, porous versions of these materials have been developed and implemented in advanced integrated circuits. Unfortunately, the mechanical properties of porous dielectrics degrade rather rapidly with increasing porosity [37]. Evidently, an OSG matrix material with a large Young's modulus and low dielectric constant would make it possible to produce porous dielectrics with superior properties.

Over the past few years, sol-gel synthesized oxycarbosilane organosilicates have emerged that possess improved mechanical properties over conventional organosilicates [9, 11, 13, 14]. This is achieved by incorporating hydrocarbon groups as bridging units to increase the network connectivity over that of earlier generations of OSG. Although promising, the improved stiffness is still far less than that of amorphous silica [13], presumably because of the significant number of terminal groups that are still present in the glass network.

In this study, we have explored how the mass density and mechanical properties of OSG correlate with the network structure of OSG. We demonstrate that the stiffness of OSG depends not only on the network connectivity, but also on the specific bridging ligaments and terminal groups. An interesting finding is that it may be possible to fabricate OSG materials with $–CH_2–$ cross-links that are significantly stiffer than amorphous silica. The elastic properties of such a material are tunable by controlling the relative concentration of$–CH_2–$ cross-links versus $–CH_3$ terminal groups. Considering for instance the ideal case where all the bridging oxygen atoms in the silica network are replaced by $–CH_2–$ cross-links, a 50% increase in bulk modulus could be obtained over pure silica, while the density is reduced by 24%. Such a material is likely to have a low dielectric constant, as the Si-C bond is less polar than the Si-O bond [3]. Even at an intermediate and probably more realistic ratio (CH_2/Si = 1), a 35% modulus improvement and 6.2% density reduction can be achieved if there are no terminal groups. Using such a material as the matrix material in a porous dielectric and assuming a power-law relationship between Young's modulus and porosity [37], dielectrics with a porosity of 40% would have a Young's modulus greater than 10 GPa. However, terminal groups always exist in real materials. They are responsible for decreased network connectivity and a rapid loss of the mechanical integrity. To attain optimum electrical and mechanical properties, further development of synthesis chemistry and remedial treatments is required to minimize the terminal group population.

5. Conclusions

We have used MD simulations to investigate the fundamental structure-property relationship of organosilicates with primary focus on the mass density and elastic properties of the material. By examining two representative classes of material models, the strengthening effects of incorporating organic cross-links in the glass network and the detrimental effects of terminal groups are modeled and discussed. Quantitative guidelines are attained for the bottom-up design of new organosilicate materials with high modulus and low dielectric constant.

Acknowledgements

HL and JJV acknowledge support from the National Science Foundation (NSF) under Grant DMR-0906892. JMK is grateful for a scholarship grant from the German research association (DFG). Assistance in part of the simulation work by Arjan Mundy is also gratefully acknowledged. We would like to thank X. Chen for help with the MD simulation software.

References

1. Grill, A. and V. Patel, *Ultralow-k dielectrics prepared by plasma-enhanced chemical vapor deposition.* Applied Physics Letters, 2001. **79**(6): p. 803-805.
2. Morgen, M., et al., *Low dielectric constant materials for ULSI interconnects.* Annual Review of Materials Science, 2000. **30**: p. 645-680.
3. Maex, K., et al., *Low dielectric constant materials for microelectronics.* Journal of Applied Physics, 2003. **93**(11): p. 8793-8841.
4. Grill, A., et al. *Optimization of SiCOH dielectrics for integration in a 90nm CMOS technology*. in *Interconnect Technology Conference*. 2004.
5. McGahay, V., et al. *65nm Cu integration and interconnect reliability in low stress k=2.75 SiCOH*. in *Interconnect Technology Conference, 2006 International* 2006.
6. Thorpe, M.F., *Continuous deformations in random networks.* Journal of Non-Crystalline Solids, 1983. **57**(3): p. 355-370.
7. Youbo Lin, et al., *PECVD low-permittivity organosilicate glass coatings: Adhesion, fracture and mechanical properties.* Acta Materialia, 2008. **56**(17): p. 4932-4943.
8. Iacopi, F., et al., *Short-ranged structural rearrangement and enhancement of mechanical properties of organosilicate glasses induced by ultraviolet radiation.* Journal of Applied Physics, 2006. **99**(5).
9. Dubois, G., et al., *Molecular network reinforcement of sol-gel glasses.* Advanced Materials, 2007. **19**(22): p. 3989-+.
10. Iacopi, F., et al., *Thermomechanical properties of thin organosilicate glass films treated with ultraviolet-assisted cure.* Acta Materialia, 2007. **55**(4): p. 1407-1414.
11. Kim, S., et al., *Organosilicate spin-on glasses - I. Effect of chemical modification on mechanical properties.* Journal of the Electrochemical Society, 2004. **151**(3): p. F37-F44.
12. Gage, D.M., et al., *Effects of UV cure on glass structure and fracture properties of nanoporous carbon-doped oxide thin films.* Journal of Applied Physics, 2008. **104**(4).
13. Rathore, J.S., L.V. Interrante, and G. Dubois, *Ultra low-k films derived from hyperbranched polycarbosilanes (HBPCS).* Advanced Functional Materials, 2008. **18**(24): p. 4022-4028.
14. Dubois, G., et al., *Superior mechanical properties of dense and porous organic/inorganic hybrid thin films.* Journal of Sol-Gel Science and Technology, 2008. **48**(1-2): p. 187-193.
15. He, H. and M.F. Thorpe, *Elastic properties of glasses.* Physical Review Letters, 1985. **54**(19): p. 2107-2110.
16. Bazant, M.Z., E. Kaxiras, and J.F. Justo, *Environment-dependent interatomic potential for bulk silicon.* Physical Review B, 1997. **56**(14): p. 8542.
17. Van Ginhoven, R.M., H. Jonsson, and L.R. Corrales, *Silica glass structure generation for ab initio calculations using small samples of amorphous silica.* Physical Review B, 2005(2): p. 024208.
18. Guttman, L. and S.M. Rahman, *Simulation of the structure of amorphous silicon dioxide.* Physical Review B, 1988. **37**(5): p. 2657.
19. Tajima, N., et al., *Carbon-doped silicon oxide films with hydrocarbon network bonds for low-k dielectrics: Theoretical investigations.* Japanese Journal of Applied Physics Part 1-Regular Papers Brief Communications & Review Papers,

2007. **46**(9A): p. 5970-5974.

20. Tajima, N., et al., *Molecular modeling of low-k films of carbon-doped silicon oxides for theoretical investigations of the mechanical and dielectric properties.* Applied Physics Letters, 2006. **89**(6).
21. Tajima, N., et al., *First-principle molecular model of PECVD SiOCH film for the mechanical and dielectric property investigation.* Proceedings of IEEE International Interconnect Technology Conference, 2005. , 2005: p. 66-68.
22. Hyuk Soon Choi, et al. *Prediction of Young's moduli of low dielectric constant materials by atomistic molecular dynamics simulation* in *Mater. Res. Soc.'05 fall meeting*. 2005. Boston: Mater. Res. Soc. .
23. Grill, A. and D.A. Neumayer, *Structure of low dielectric constant to extreme low dielectric constant SiCOH films: Fourier transform infrared spectroscopy characterization.* Journal of Applied Physics, 2003. **94**(10): p. 6697-6707.
24. Lin, Y.B., T.Y. Tsui, and J.J. Vlassak, *Octamethylcyclotetrasiloxane-based, low-permittivity organosilicate coatings - composition, structure, and polarizability.* Journal of the Electrochemical Society, 2006. **153**(7): p. F144-F152.
25. Sun, H., *COMPASS: An ab initio force-field optimized for condensed-phase applications - Overview with details on alkane and benzene compounds.* Journal of Physical Chemistry B, 1998. **102**(38): p. 7338-7364.
26. Huff, N.T., et al., *Factors affecting molecular dynamics simulated vitreous silica structures.* Journal of Non-Crystalline Solids, 1999. **253**: p. 133-142.
27. Andersen, H.C., *Molecular-dynamics simulations at constant pressure and-or temperature.* Journal of Chemical Physics, 1980. **72**(4): p. 2384-2393.
28. Parrinello, M. and A. Rahman, *Polymorphic transition in single-crystals - a new moleculear-dynamics method.* Journal of Applied Physics, 1981. **52**(12): p. 7182-7190.
29. Weiner, J.H., *Statistical mechanics of elasticity*. 1983, New York: John Wiley
30. Ewald, P.P., *The calculation of optical and electrostatic grid potential.* Annalen Der Physik, 1921. **64**(3): p. 253-287.
31. Verlet, L., *Computer experiments on classical fluids .I. thermodynamical properties of Lennard-Jones molecules* Physical Review, 1967. **159**(1): p. 98-&.
32. *Materials Studio*, Accelrys, Inc.
33. Mauri, F., et al., *Si-O-Si bond-angle distribution in vitreous silica from first-principles Si-29 NMR analysis.* Physical Review B, 2000. **62**(8): p. R4786-R4789.
34. Mozzi, R.L. and B.E. Warren, *Structure of vitreous silica.* Journal of Applied Crystallography, 1969. **2**: p. 164-&.
35. Neuefeind, J. and K.D. Liss, *Bond angle distribution in amorphous germania and silica.* Berichte Der Bunsen-Gesellschaft-Physical Chemistry Chemical Physics, 1996. **100**(8): p. 1341-1349.
36. Jan M. Knaup, H.L., Joost J. Vlassak, and Efthimios Kaxiras, *Elastic properties of dense organosilicate glasses dependent on the C/Si ratio*, in *Silicon Carbide and Related Materials 2009*. 2010, Trans Tech Publications, Switzerland: Nürnberg, Germany. p. 267-270.
37. Li, H., et al., *The effect of porogen loading on the stiffness and fracture energy of brittle organosilicates.* Journal of Materials Research, 2009. **24**(1): p. 107-116.
38. Tsui, T.Y., et al., *The effect of elastic modulus on channel crack propagation in organosilicate glass films.* Thin Solid Films, 2006. **515**(4): p. 2257-2261.
39. *NIST property data summaries*, National Institute of Standards and Technology, http://www.ceramics.nist.gov/srd/summary/SiO2.htm.

40. Yuan, C.A., et al., *Chemical-mechanical relationship of amorphous/porous low-dielectric film materials.* Computational Materials Science, 2008. **42**(4): p. 606-613.
41. Allinger, N.L., Y.H. Yuh, and J.H. Lii, *Molecular mechanics - the MM3 force-field for hydrocarbons .1.* Journal of the American Chemical Society, 1989. **111**(23): p. 8551-8566.

Figures

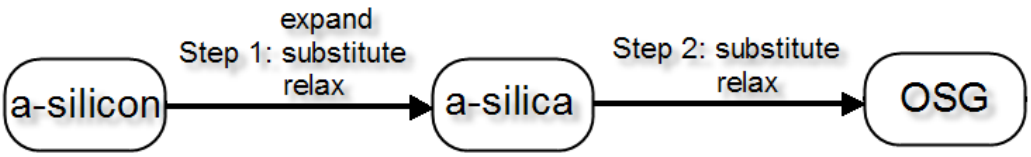

Figure 1. Flowchart for generating the type-I and type-II OSG models.

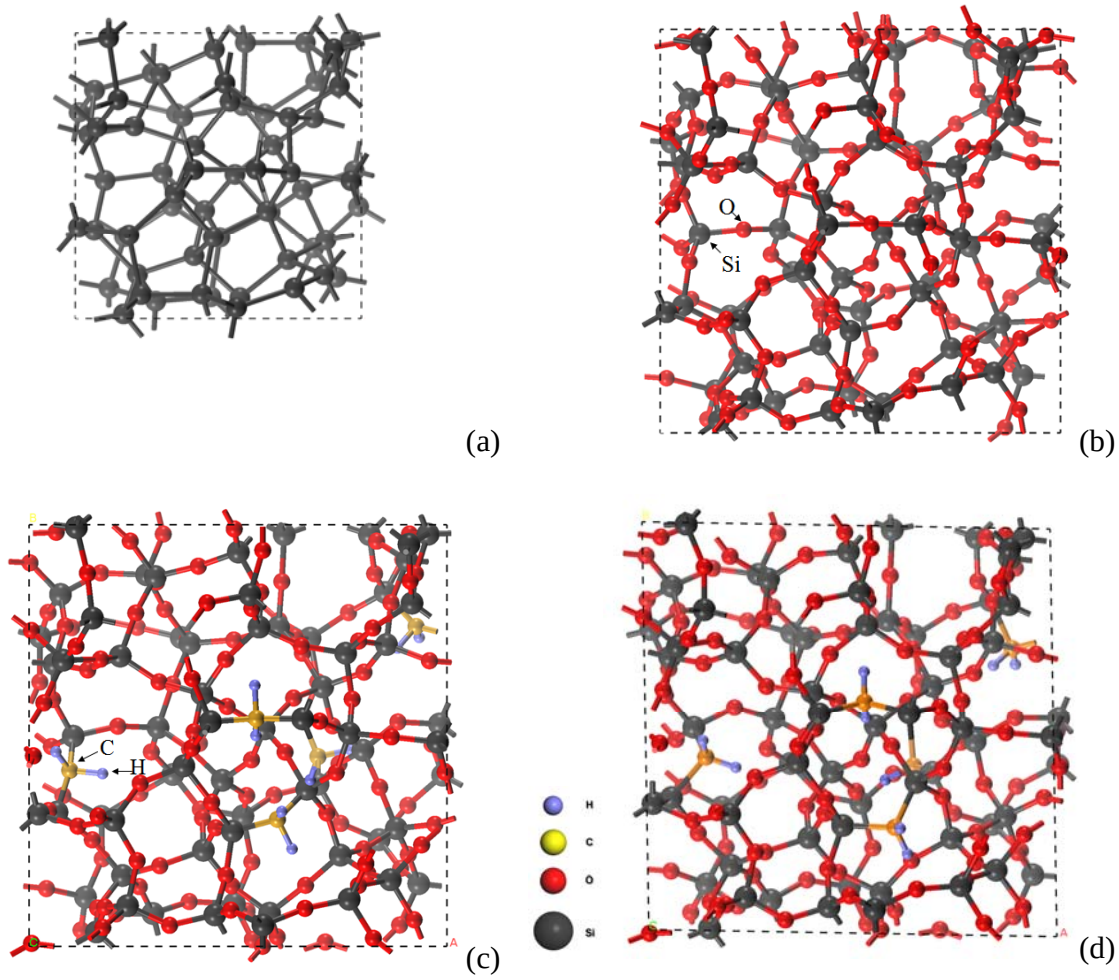

(a) (b) (c) (d)

Figure 2. Unit cell of (a) amorphous silicon with 64 Si atoms, (b) silica derived from (a), (c) type-I OSG with five methylene cross-links, and (d) relaxed OSG from Fig.2c.

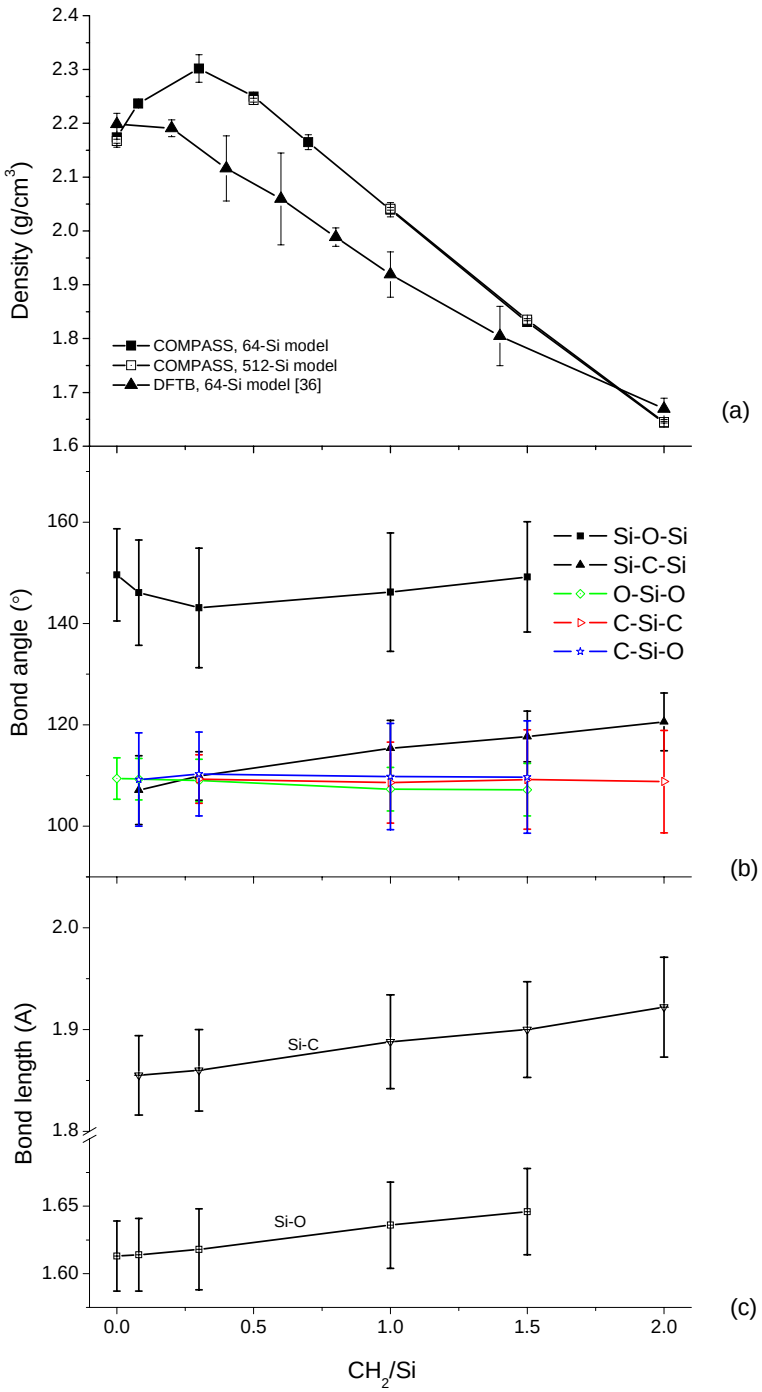

Figure 3. (a) Mass density of type-I OSG, (b) various bond angle and (c) bond length as a function of CH_2/Si ratio. The error bars denote one standard variation.

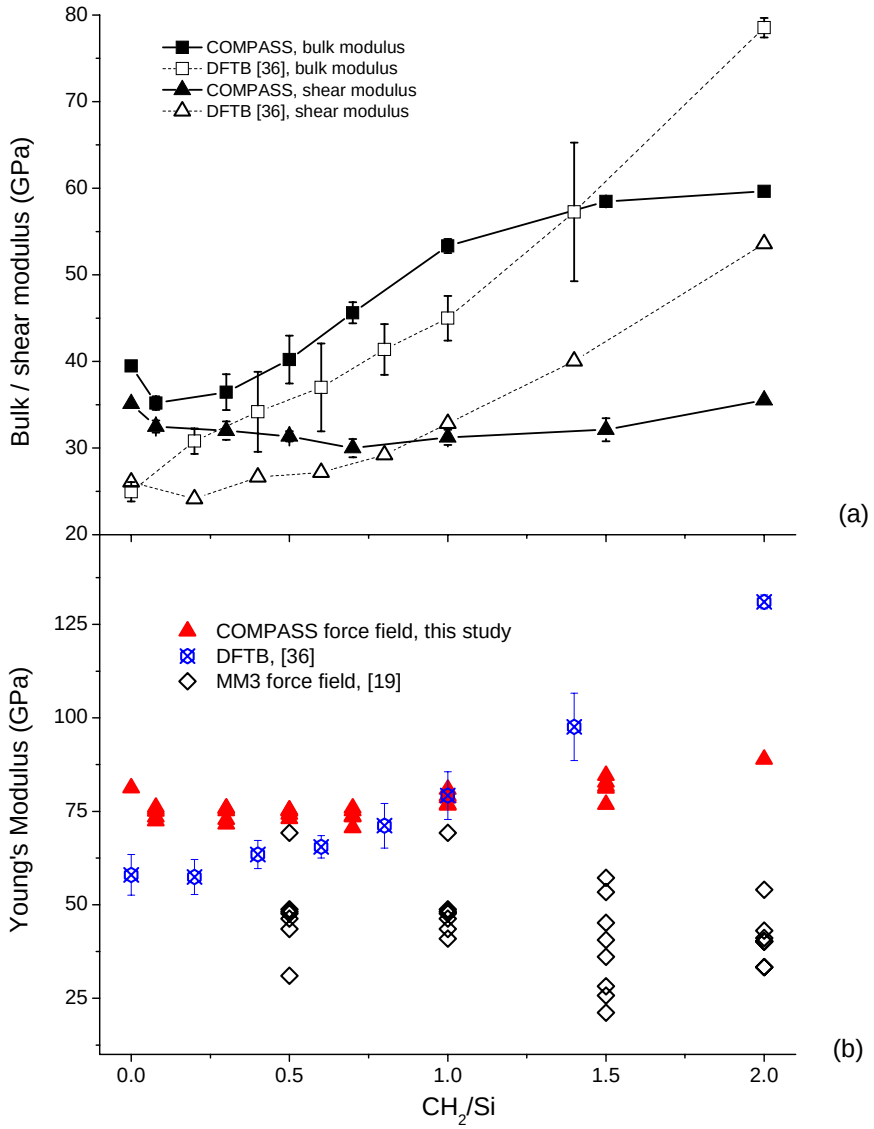

Figure 4. (a) Bulk modulus and shear modulus, and (b) Young's modulus of type-I OSG as a function of CH_2/Si ratio for different potentials.

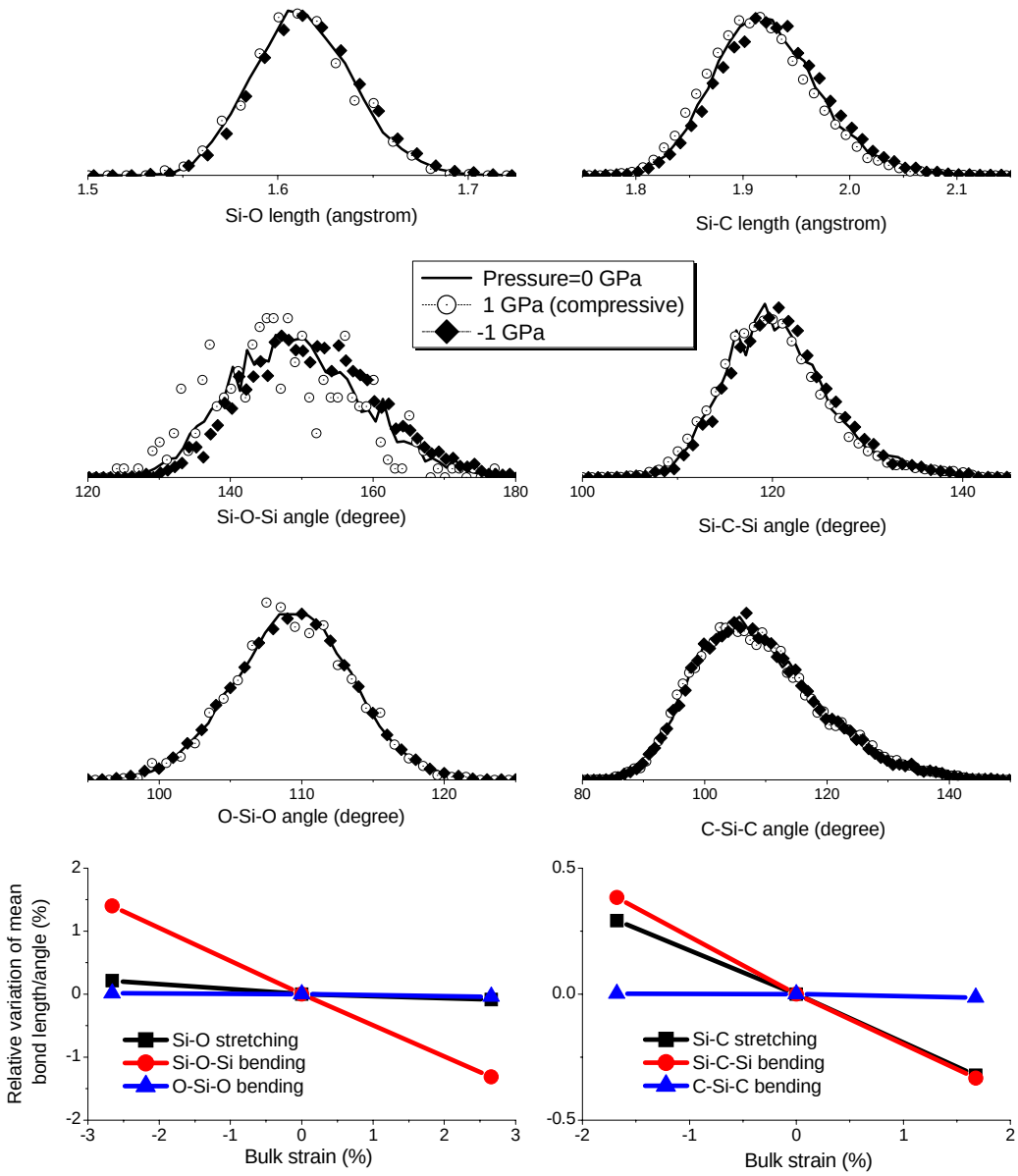

Figure 5. Evolution of bond length and angle distribution in SiO_2 (left panels) and $Si(CH_2)_2$ under hydrostatic loading.

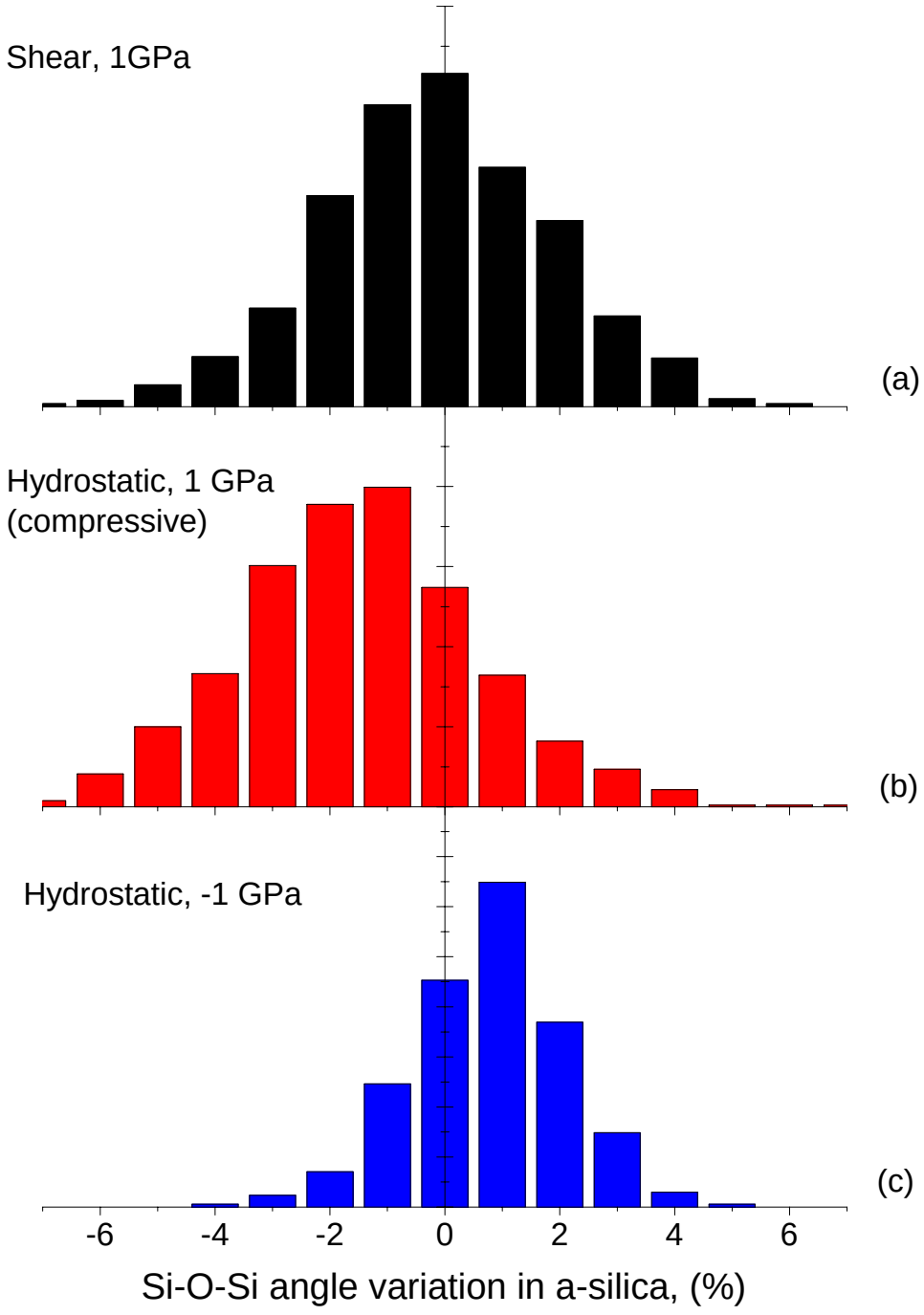

Figure 6. The distribution of the relative change of the Si-O-Si angles in silica under (a) a shear stress of 1GPa, (b) hydrostatic pressures of 1 GPa (compressive), and (c) hydrostatic pressures of -1 GPa.

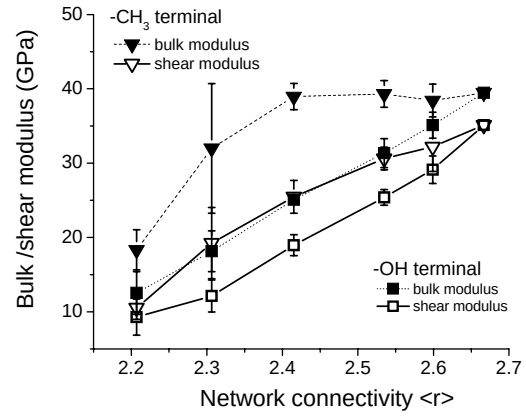

(a)

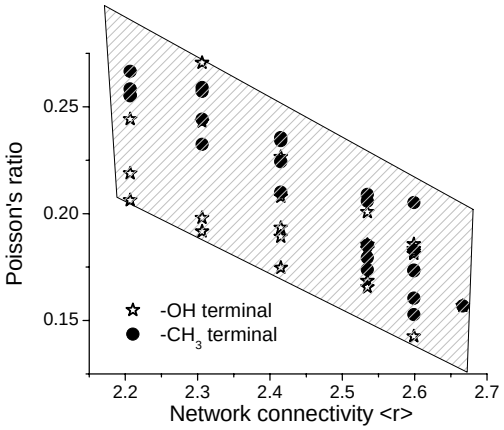

(b)

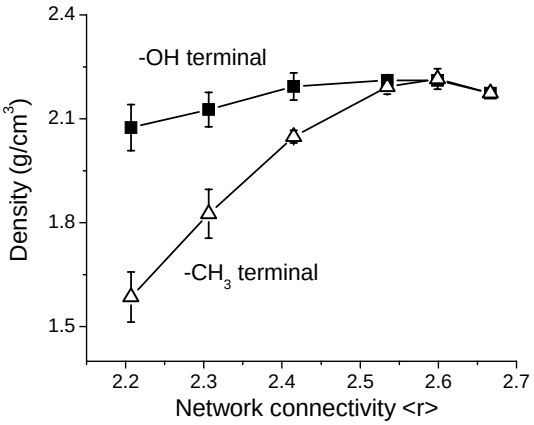

(c)

Figure 7. (a) The bulk and shear modulus, (b) Poisson's ratio, and (c) density of type-II OSG as a function of network connectivity.

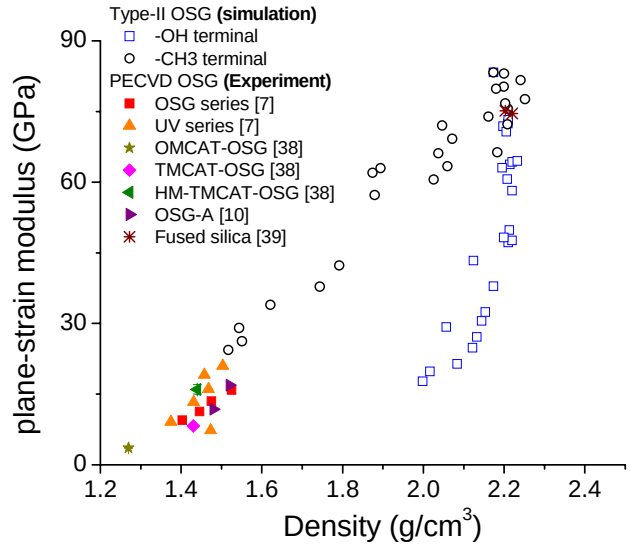

(a)

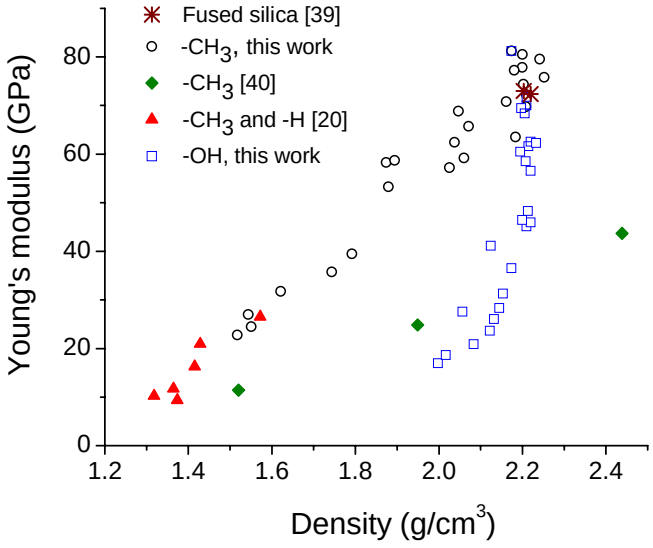

(b)

Figure 8. (a) Plane-strain modulus and (b) Young's modulus of type-II OSG as functions of density, compared with similar materials and models from experiment (a) and MD simulations (b), respectively.